

Predictive modeling for runaway electron avoidance and mitigation

Theory Performance Target Final Report

Dylan Brennan, Nathaniel Ferraro, Stephen Jardin, Chang Liu, and Chen Zhao
Princeton Plasma Physics Laboratory

Matthew Beidler, Diego del-Castillo-Negrete, and Guannan Zhang
Oak Ridge National Laboratory

Luis Chacon, Xianzhu Tang, William Taitano, and Don Daniel
Los Alamos National Laboratory

Robert Harvey and Yuri Petrov
CompX

Charlson Kim
SLS2 Consulting

Lang Lao, Yueqiang Liu, Joseph McClenaghan, and Paul Parks
General Atomics

Christopher McDevitt
University of Florida

Allen Boozer
Columbia University

Mark Adams
Lawrence Berkeley National Laboratory

Boris Breizman and Irene Gamba
University of Texas, Austin

Matthew Knepley and Joseph Pusztay
University at Buffalo

(Dated: October 29, 2021)

CONTENTS

I. Executive Summary	3
II. The Goals of the Performance Target and the Report	4
III. Modeling of a DIII-D SPI experiment	5
IV. Investigation of hot-tail runaway electron seed generation during thermal quench with the iRFP kinetic code	6
A. A Comparison with NORSE and CCPWRS	7
B. Investigation of Dreicer generation rate dependence on plasma temperature in realistic tokamak geometries with the 2D-2P iRFP	8
V. Investigation of the runaway electron seed production dependence on radial transport in dynamics scenarios using the BMC code	10
VI. Runaway dissipation by secondary material injection in ITER relevant scenarios using the RAMc code	12
VII. Coupling NIMROD and CQL3D to study RE generation in a DIII-D discharge	13
VIII. Runaway mitigation, transport and synchrotron modeling using KORC	18
A. KORC modeling of RE mitigation using high-Z impurity injection	18
B. Coupling KORC with extended-MHD codes	22
1. KORC coupling with NIMROD	22
2. KORC coupling with M3D-C1	23
C. Synchrotron modeling with KORC	25
IX. Summary	28
References	29

I. EXECUTIVE SUMMARY

The focus of the 2021 Theory Performance Target was centered on understanding the runaway electron seed generation during thermal collapse disruptions in tokamaks. Understanding and being able to accurately simulate this process is critically important to being able to avoid and or mitigate their generation. Analysis of disruption scenarios generally involves several different areas of expertise, in this case including the physics of the disrupting plasma, the relativistic kinetic physics of the driven runaways, and the substantial complexity of the computational methods involved in their simulation. This project has involved significant contributions from the SCREAM SciDAC team, including simulations with the BMC[1], CCPWRS[2], CQL3D[3], iRFP[4], KORC[5], NIMROD[6], NORSE[7], M3D-C1[8], and RAMc[9] codes, among others.

The physics involved is captured in part by reduced modeling, such as simulations assuming a homogeneous plasma, and yet strongly influenced by the complex 3D structure and dynamics in a disruption, which are only beginning to be captured accurately in MHD simulations. To advance our understanding of how and to what extent runaway electrons are driven in disruptions, we must accurately simulate all of the most important physics mechanisms governing the seed generation. A great deal of progress toward this goal has been made in this project.

In short summary, a number of technological advances were achieved and several theoretical projections were made for future experiments such as ITER, in addition to a few key findings from analyses of experimental discharges on DIII-D and JET. In an analysis of one DIII-D experiment, the reasons for a lack of observed runaway generation are shown to be due to both a low initial temperature and moderately slow thermal collapse rate, and significant radial transport of the runaway seed due to field perturbation and stochastic fields. In another study, the differences between observed power fluxes to the walls and runaway electron divertor strike patterns in DIII-D and JET discharges are detailed via simulations.

Although the SCREAM project has made major strides in the simulation and in the understanding of the physics of runaway electrons (RE), the threat to the ITER mission remains and work to address this threat must continue. The statement made by Breizman, Aleynikov, Hollmann, and Lehnen in their 2019 Nuclear Fusion review remains true: “With ITER construction in progress, reliable means of RE mitigation are yet to be developed. This is an essential part of the disruption mitigation strategy. Although theoretical and experimental understandings of REs behavior in current tokamaks have progressed significantly during the last decade, large uncertainties remain with respect to runaway control in ITER. A part of this challenge is to reconcile the physics and engineering constraints, as explained in section 11 of this review.”

The runaway seed electron problem is inherently a multiscale problem dependent on time history of the discharge through a thermal collapse. Accurate quantitative calculations of the runaway generation in experiment require challenging nonlinear simulations, and preeminent interpretation of them. Despite the achievements described here, much more needs to be done to successfully predict how the runaways will be avoided and mitigated in experiments such as ITER.

II. THE GOALS OF THE PERFORMANCE TARGET AND THE REPORT

This report summarizes work conducted for the 2021 Theory Performance Target over the entire project from Oct 1, 2020 to Sep 30, 2021. The description of the target is as follows:

Disruptions in tokamaks occur when the control of confined thermal energy is suddenly lost as the plasma becomes unstable, causing the plasma to undergo a thermal collapse. As the plasma rapidly cools, a large electric field is induced which can cause “runaway” acceleration of a small population of “seed” electrons that are above a critical energy. In future fusion reactors and burning plasma experiments, including ITER, these runaway electrons can reach multi-MeV energies and damage the device severely, threatening the viability of experimental operations. To avoid and mitigate runaway electrons we must understand how the seed electron population depends on the time history of the discharge through the thermal collapse disruption. In FY 2021, simulations will be performed with a suite of codes including kinetic and magnetohydrodynamic (MHD) models, to investigate the generation of the seed runaway electrons and their subsequent acceleration. These simulations will probe the dependence of the runaway seed population on the time history of realistic scenarios of thermal collapse and electric field, and investigate possible mitigation techniques to control their energies.

The goals for all four quarters are:

Q1: October 1st – December 31st 1) We will conduct thermal collapse simulations with the iRFP and NORSE codes, simulating hot tail formation under radiative cooling. The simulated conditions will be comparable to pre-existing 3D MHD thermal collapse simulations, forming the basis for model verification. The dissipation of RE using high-Z impurities in DIII-D will be modeled using KORC incorporating collision operators for partially ionized impurities, time evolving electric and magnetic fields, and spatiotemporal models of impurities.

Q2: January 1st – March 31st 2) Varying rates of thermal collapse will continue to be investigated in a series of phase space simulations, to inform the 3D simulations on what seeds are predicted. The iRFP code will be used for studying the Dreicer seed formation mechanism. MHD simulations using M3D-C1 and NIMROD will be analyzed to investigate the time dynamics of the thermal collapse rate and effect of MHD instabilities and stochastic fields on seed formation. The dependence of the RE seed production rate on the radial and temporal evolution of the electric field, the temperature, and density will be studied using the Backward Monte Carlo (BMC) method. KORC will simulate RE transport in stochastic magnetic fields obtained from 3D MHD simulations. RAMc simulations will be performed to assess RE dissipation by secondary material injection in ITER relevant scenarios.

Q3: April 1st – June 30 3) Informed by the previous studies, 3D simulations of seed generation through the thermal quench will become the focus. The sufficiency of coupling from NIMROD to CQL3D to provide initial distributions of prompt RE electrons will be investigated. We will run KORC and CQL3D with impurity profiles from M3D-C1 and NIMROD MHD simulations to study effect in 3D impurity fields. The RAMc code will be used for a full Ohmic-to-runaway conversion simulations, where for a given thermal cooling

history, we will study the phase space evolution of runaways and the Ohmic to runaway current conversion with/without impurity injection.

Q4: July 1st – September 30th 4) Self-consistent simulations including thermal quench with impurities injection, seed formation, RE-MHD coupling and MHD instabilities will be conducted using M3D-C1 or NIMROD. The polarization of synchrotron emission by RE will be studied using the KORC synthetic diagnostic.

The individual goals of all four quarters, and thus the whole project, have been met. Although, a great deal of further work remains to be done to meet the goals laid out in Ref. [10]. In this report we first briefly review the context of the project and the runaway seed electron problem in Sec. III, and highlight the focus on a specific DIII-D experiment where a disruption is triggered with Shattered Pellet Injection (SPI). In Sec. irfp we discuss the analysis with the IRFP code, including a comparison with the runaway seed generation from the NORSE code, and a Dreicer seed generation in toroidal geometry. Section V investigates the dependence on radial transport of the Dreicer and hot tail seed runaway electron production using the BMC (Backward Monte Carlo) code. In Sec. VI we describe results with the RAMc code, where runaway dissipation with impurity injection was investigated in configurations similar to this DIII-D experiment. Next, in Sec. VII we present the results of coupling CQL3D and NIMROD to study the runaway dissipation in simulations of a specific DIII-D discharge from that experiment. Next, in Sec. VIII we describe the coupling of KORC to nonlinear MHD codes NIMROD and M3D-C1, in analysis of the confinement of runaways in the perturbed magnetic fields and impurities, and the effect on the wetted area of the diverter. Also presented are results from a synthetic synchrotron diagnostic in KORC, clarifying the physics behind the experimental observations. Last, in Sec. IX we briefly review some of the findings from the project, and highlight some future directions for the research.

III. MODELING OF A DIII-D SPI EXPERIMENT

A large part of the modeling effort was focused on a DIII-D SPI experiment where an initially $2keV$ plasma was induced into a disruption with SPI. Initial simulations of the SPI and subsequent MHD were conducted[11] in advance of the project start, providing for a good basis on which to extend the simulations to include runaway electron physics. The simulations are modeled after DIII-D discharge 160606 in Ref. [12], and generally capture the thermal collapse and SPI dynamics.

Efforts with reduced modeling were conducted to initially characterize and clarify the physics regimes of the experiment. Simulations included similar conditions to the experiment with different codes, forming a central theme. In addition, scoping studies with reduced models served to support the larger simulation efforts in that they gave context to the results from the MHD simulations coupled with kinetic runaway modeling.

For example, the initial and final temperatures, and the rate of thermal collapse, are key aspects determining how much of a runaway seed is generated. The scoping studies showed the hot tail is formed generally more substantially as the thermal collapse time decreases to

be on the order the characteristic electron collision time of the pre-thermal collapse plasma. It was found that since this timescale becomes extremely short, tens of microseconds, for the 2keV plasma of the experiment, the seed generation was expected to be small and requiring avalanche generation over the longer current quench timescale to form a large population of runaways.

The interaction of the runaways with 3D magnetic fields and impurity density was also part of the focus. It was found that the magnetic field contained significant stochastic regions for long enough to de-confine and lose much of the runaways that were generated. Thus the two aspects of the temperature collapse dynamics and the stochastic magnetic field simultaneously acted in experiment to prevent the runaway seed formation.

This result is consistent with simulation results from several codes as indicated below, as well as the experiment. Future case studies will include more substantial runaway electron seed generation in experiment, but the current case study has proved highly informative in finding agreement on when the seed population is modest, and providing at least some explanations as to why the runaway population did not avalanche significantly in the experiment.

IV. INVESTIGATION OF HOT-TAIL RUNAWAY ELECTRON SEED GENERATION DURING THERMAL QUENCH WITH THE IRFP KINETIC CODE

LANL researchers have developed semi-Lagrangian 2D-2P (two spatial dimensions and two momenta) nonlinear relativistic Vlasov-Fokker-Planck (VFP) simulation tool (IRFP [4, 13]) to model runaway-electron dynamics in realistic magnetic fields in toroidal geometry, and arbitrary plasma temperatures. During the project the capability of iRFP was enhanced by including a self-consistent electric field evolution via Ohm's law. The new capability was exercised to model the thermal quenching of hot electrons in tokamaks and the initial phase of runaway electron generation. The process begins with a sudden loss of plasma energy due to radiative cooling by shattered pellet injection (SPI), which leads to a thermal quench. The rapid plasma cooling, in turn, increases the plasma resistivity, amplifying the electric field (via Ohm's law) and leading to the acceleration of a certain fraction of the thermal bulk population to relativistic energies (hot-tail runaway seed).

In this study, we consider a prescribed time-dependent cooling rate, and study the runaway seed for different initial plasma temperatures and thermal-quench timescales. For this purpose, we consider a linearized electron-electron collision based on a prescribed background temperature and number density. We also consider a Lorentz (pitch-angle scattering) model for the electron-ion interaction and ignore any radiation reaction forces.

The simulation begins by evolving to steady-state two initially stationary Maxwell-Juttner distributions with a temperature T_0 (3keV and 10keV) and a number density n_0 ($10^{20}m^{-3}$). The simulation is run with an imposed, static, below-critical electric field E_0 ($1.98 \times 10^{-4}V/m$ and $1.20 \times 10^{-3}V/m$), which results in a steady-state Spitzer current j_0 ($10^6 Amp/m^2$), satisfying Ohm's law, $E_0 = \eta(T_0)j_0$, with $\eta(T) \propto T^{-3/2}$ the Spitzer resistivity. We note that, for the given plasma conditions, the relativistic collision-time scale is

$\tau_{c,rel} = 3.35 \times 10^{-2} s$, the critical field is $E_{crit} = 5.1 \times 10^{-2} V/m$ and the reference current is $j_{crit} = en_0c = 4.8 \times 10^9 Amp/s$.

A. A Comparison with NORSE and CCPWRS

A similar study was conducted with the NORSE[7] and CCPWRS[2] codes. NORSE is a relativistic kinetic code which models a homogeneous plasma with a finite difference solver, is not fully conservative, and yet includes the important effects of nonlinear electron-electron collisions and self-consistent inductive electric field. The code CCPWRS (Conservative Collisional Particle-Wave Resonance System) has been developed in 3D with cylindrical coordinates and is capable of including the particle kinetic transport equation with a time dependent electric field term, as well as collisional forms such as the relativistic Fokker-Planck-Landau (FPL) operator, and the quasilinear diffusion terms. The incorporated numerical module for particle-wave resonance modeling makes CCPWRS one of the few existing codes capable to compute any kind of resonance wave mode. In addition, the code strictly preserves both mass and energy of the system. In numerical experiments, the anisotropic diffusion of particles in momentum space can be clearly observed under strong magnetization.

As is done in the NORSE and CCPWRS results, simulations with iRFP are restarted from the initial steady-state conditions with a time-dependent exponentially decaying background temperature profile, $T = T_0 \exp(-t/\tau_{TQ})$ until $T(t = t_f) = 20eV$. Here, t_{TQ} is the thermal-quench time-scale. The evolution of the background temperature affects electron-electron collisions via the corresponding (linearized) collisional potentials, and the electric field via Ohm's law, $E = \eta(T)(j_0 - j_{seed})$. The seed current, $j_{seed} = \int_{p \notin \Omega_{bulk}} p f d^3p$, is computed by excluding the distribution function's region pertaining to the bulk population, $\Omega_{bulk} \in [0, p_{bulk}]$, where $p_{bulk} = 0.1 m_e c$ in this study.

As in the NORSE and CCPWRS results, we consider thermal quench time-scales ranging from $0.15 ms$ to $1 ms$. The resulting seed density, $\rho_{seed} = \int_{p \notin \Omega_{bulk}} f d^3p$ are plotted in Fig. 1, together with the NORSE results. As can be seen, iRFP reproduces qualitatively all the features found with NORSE and CCPWRS. Minor quantitative differences are expected due to differences in the thermal cooling treatment (NORSE treats the cooling process via a conservative heat sink operator instead of a thermal background), as well as the different electric field evolution equation (NORSE employs an inductive model instead of a Spitzer one). The CCPWRS model includes a time dependent seeded E-field varying in time, emulating the thermal quench, and the relativistic FPL operator. The CCPWRS result is very similar similar to that of NORSE and iRFP as shown in Fig. 2. Given the model disparity, we conclude that the seeding behavior reported by NORSE, CCPWRS and iRFP is in fact a robust mechanism.

It is also clear from this that it is important to correctly capture both the spatial dependence of the generation, not in the least because of the range of the initial temperature profile, but also the wide range of timescales. This was the main motivation for the study of the Dreicer generation with the iRFP code.

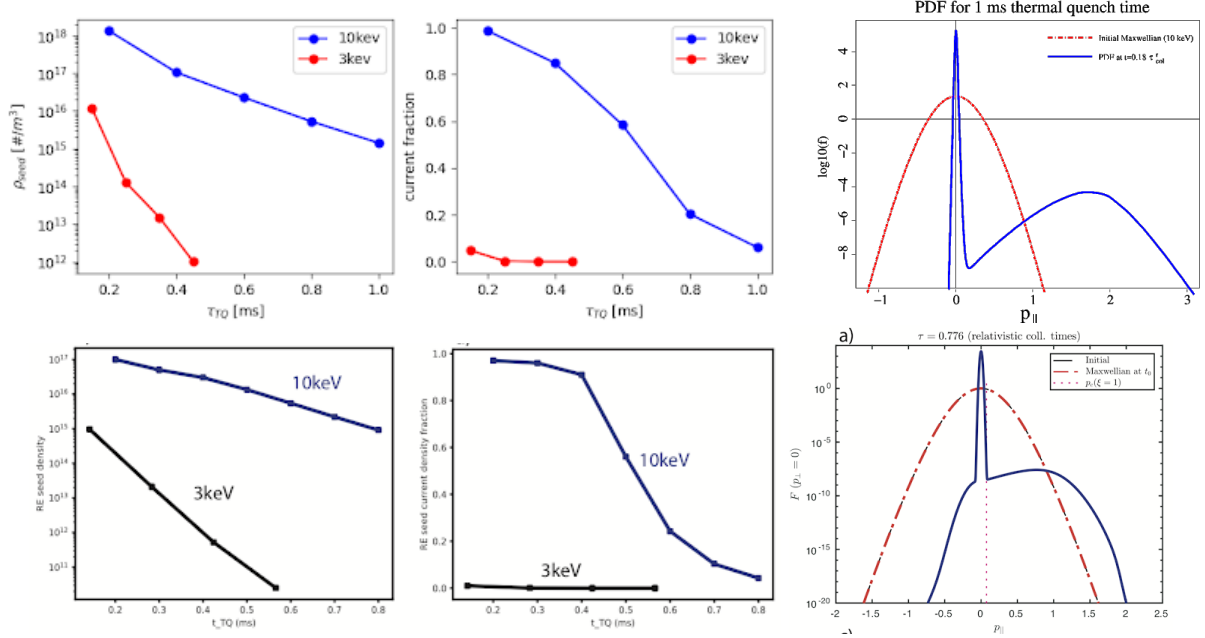


FIG. 1. The seed density (left) and seed current fraction (center) for 10 keV and 3 keV initial plasmas for iRFP (top) and NORSE (bottom). The values are plotted for various imposed thermal-quench timescales, τ_{TQ} . The initial and final distribution functions are also shown (right). iRFP's final distribution is depicted for the 1ms thermal quench time when the background temperature reaches 20eV (at 6.2ms, or ~ 0.18 relativistic collision times).

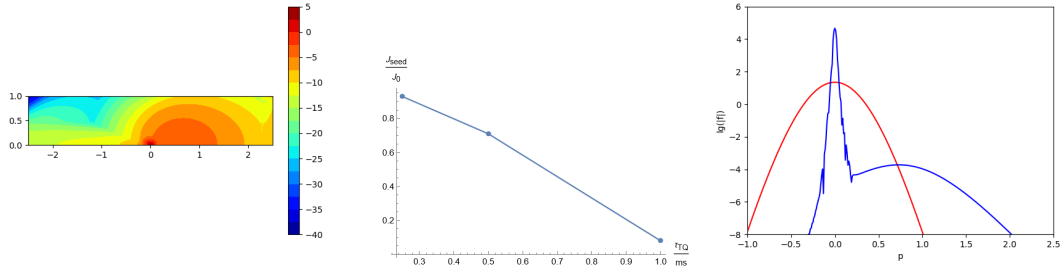


FIG. 2. The particle distribution f at a time after the thermal quench in the simulation (a), the runaway seed current density as a function of thermal quench rate (b), and the initial and final parallel distribution functions in a simulation from the CCPWRS code (to be compared with Fig. 1).

B. Investigation of Dreicer generation rate dependence on plasma temperature in realistic tokamak geometries with the 2D-2P iRFP

The iRFP code [4, 13] was used to study the impact of plasma temperature on the Dreicer runaway-electron generation rate in realistic toroidal geometries, confirming the conclusions of an earlier study[14]. Violent temperature and magnetic-field evolution in a tokamak disruption demand the ability to simulate runaway electrons (RE) in arbitrary 3D

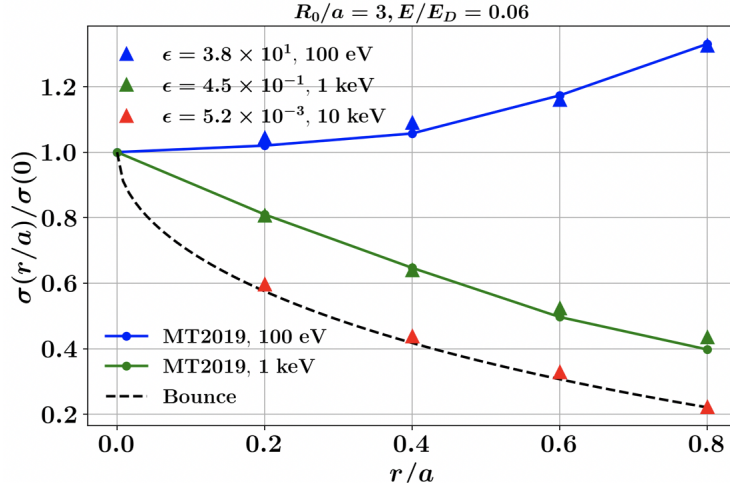


FIG. 3. Relative Dreicer RE generation rate vs toroidal radius in a 2D toroidally symmetric magnetic geometry for various plasma temperatures (corresponding to different asymptotic parameters ϵ , defined as the ratio of the thermal bounce time to the thermal collision time). Triangles are the results of our novel algorithm. Dashed line denotes the bounce-averaged solution for hot plasmas. Lines are the solutions found with a particle method in Ref. [14]. It can be seen that our approach matches results in different regimes perfectly.

magnetic fields and plasma temperatures. However, to date, most kinetic RE simulation tools are able to deal only with nested magnetic flux surfaces and sufficiently hot plasmas. This research demonstrates an efficient algorithm in toroidal geometry suitable for arbitrary plasma temperatures, so far demonstrated on nested flux surfaces but that can be readily extended to arbitrary 3D magnetic fields. The approach has been applied to the problem of Dreicer runaway generation in toroidal geometry with varying plasma temperatures, and has confirmed the results of an earlier study[14].

Fast electron bounce times, infrequent collisions, and relativistic speeds pose a significant challenge for RE modeling in realistic geometry. Researchers at LANL have implemented a novel asymptotic-preserving algorithm in the iRFP LANL code that is able to accurately capture fast electron motion while following slower collisional time scales. The approach employs our recently developed fully nonlinear conservative relativistic Fokker-Planck collision algorithm [4], and a novel Green’s function method to integrate collisional effects along electron orbits or arbitrary complexity, including fully stochastic magnetic fields. The approach has been verified against recent simulations in [14] of the impact of plasma temperature on the Dreicer runaway-electron generation rate in nested toroidal flux surfaces, demonstrating excellent quantitative agreement (see Fig. 3). In particular, the simulations confirm the strong impact of plasma temperature on the Dreicer generation rate, and the need to carefully consider both arbitrary magnetic field geometries and realistic plasma temperatures in these studies. Additionally, these results highlight the ability of the method to deal with both weakly and strongly collisional limits seamlessly.

In Fig. 4 is shown a convergence study in $\Delta t/\epsilon$ (with ϵ the ratio of thermal collision time

to thermal bounce time) indicates uniform convergence for arbitrary values of this parameter ($\Delta t/\epsilon \gg 1, \Delta t/\epsilon \ll 1$). This demonstrates the ability of the approach to capture arbitrary plasma collisionalities. In particular, the errors behave as predicted by analysis ($O(\Delta t)$ for $\Delta t/\epsilon \gg 1$).

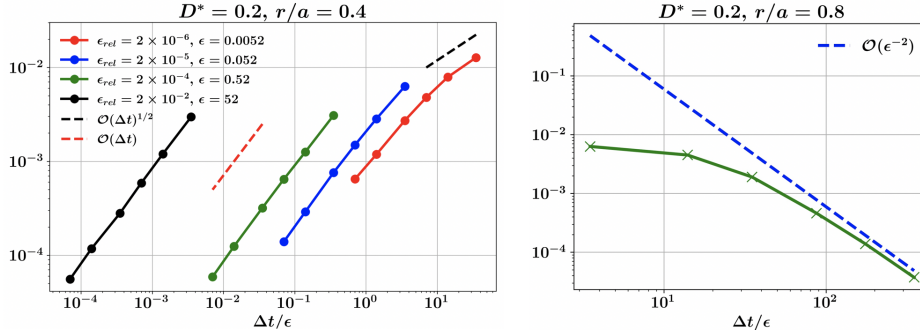


FIG. 4. The relative error at very small (left) and very large (right) $\Delta t/\epsilon$, showing convergence in both regimes.

V. INVESTIGATION OF THE RUNAWAY ELECTRON SEED PRODUCTION DEPENDENCE ON RADIAL TRANSPORT IN DYNAMICS SCENARIOS USING THE BMC CODE

The BMC (Backward Monte Carlo) code developed at ORNL [1] has been recently extended and optimized [15, 16] to perform accurate and efficient computations of RE generation in fully time dependent dynamic scenarios including radial transport. Up to now, most studies on Dreicer and hot tail generation have either neglected radial transport or limited attention to non-chaotic magnetic fields. However, MHD simulations have revealed the ubiquity of magnetic field stochasticity during the thermal quench. Motivated by this, we have used the BMC upgraded code to perform a systematic parameter scan in order to understand the dependence of the seed production on different physics mechanisms in the presence of radial diffusion caused by magnetic field stochasticity [17]. The diffusion model is based on the Rechester-Rosenbluth quasilinear diffusion model in stochastic magnetic fields, modulated in space to describe the edge stochasticity observed in MHD simulations. In addition, a momentum dependence is included in the diffusivity to account for the numerically observed suppression of radial transport of highly energetic electrons.

There are many parameters involved in the modeling and simulation of the production rate of seed runaway electrons, including the initial and final temperature of the plasma, the rate of thermal collapse, the plasma density, the electric field, the Z value of the impurities, and the dependence on radial transport, among others. Understanding the dependence of the seed generation on these parameters is a critical first step to assess the potential risk RE avalanche generation. Since the BMC focuses directly on the computation of the runaway probability and the seed production, rather than in the costly computation of the

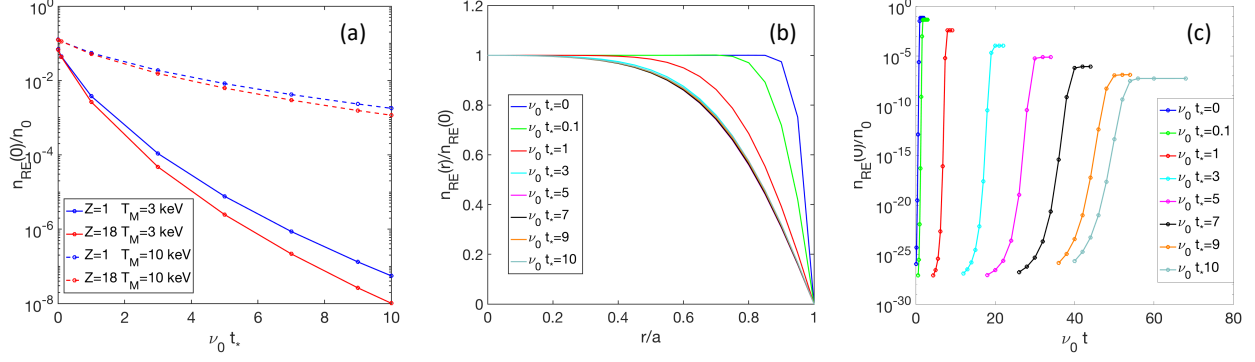


FIG. 5. Dependence of seed runaway electron density on thermal quench time scale, t_* , computed with the BMC code. Panel (a) shows the seed density at the magnetic axis, $n_{RE}(0)$, normalized with the plasma density, n_0 , as function of $\nu_0 t_*$, where ν_0 is the thermal collision frequency, for different values of Z and initial plasma temperatures T_M . Panel (b) shows the radial dependence of the seed density as function of r , normalized by the value at $r = 0$, for different values of $\nu_0 t_*$, with $Z = 1$ and $T_M = 3\text{keV}$. Panel (c) shows the time evolution of the seed density at $r = 0.5$ for different values of $\nu_0 t_*$, with $Z = 1$ and $T_M = 3\text{keV}$. In all these simulation $E_0 = 10^{-3}$, $D_0 = 0.01$, and $\Delta p = 2$.

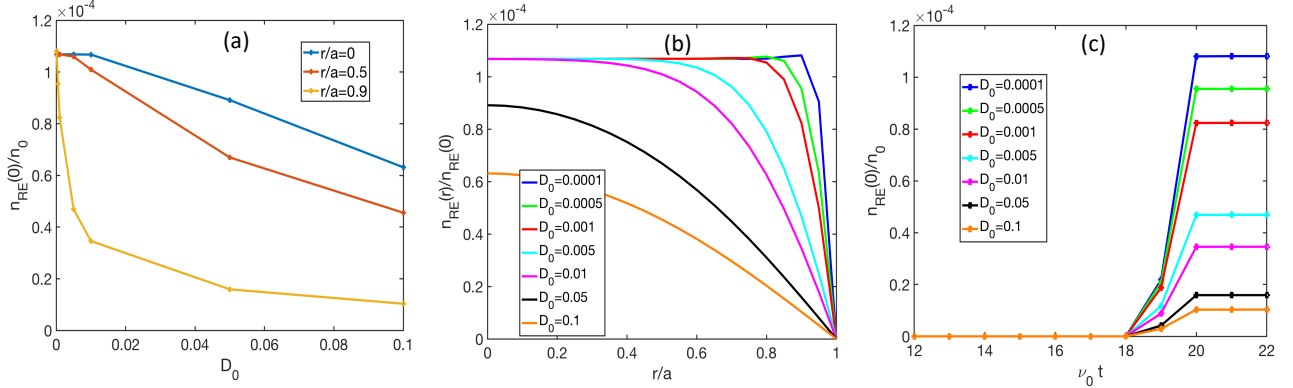


FIG. 6. Dependence of seed runaway electron density on normalized constant radial diffusivity D_0 . Panel (a) shows the seed density at the magnetic axis, $n_{RE}(0)$, normalized with the plasma density, n_0 , as function of D_0 at different radii. Panel (b) shows the seed density as function of r , normalized by the value at $r = 0$, for different values of D_0 . Panel (c) shows the time evolution of the seed density at $r = 0$ normalized with the plasma density, n_0 , for different values of D_0 . In all these simulations, $Z = 1$, $\nu_0 t_* = 3$, $T_M = 3\text{keV}$, $E_0 = 10^{-3}$, and $\Delta p = 2$.

whole 3D+time distribution function, it is a suitable computational tool to perform fast parameter scans. In particular, since the probability of runaway provides a Greens-type function, the BMC decouples the computation of the production rate from the specifics of the initial distribution function. That is, for a given thermal quench scenario, a single BMC calculation can be used to explore the seed generation for different initial electron distributions.

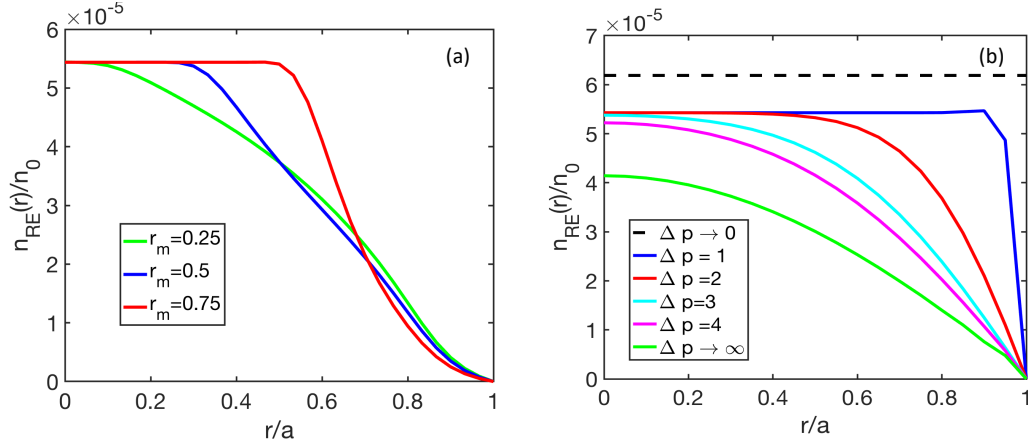


FIG. 7. Seed runaway electron density as function of r for different radial profiles (a), and different momentum dependences (b) of the radial diffusivity. The parameter r_m determines the boundary of the stochastic magnetic field, and the parameter Δp determines the strength of the momentum dependent diffusion suppression. In all these simulations, $Z = 1$, $\nu_0 t_* = 3$, $T_M = 3\text{keV}$, $E_0 = 10^{-3}$ and $D_0 = 0.01$.

The simulations presented assume an exponential thermal quench with a cooling time scale t_* , and the electric field is obtained from Ohm's law using a Sptizer resistivity, temperature dependent, model. The time has been normalized using the thermal collision frequency, ν_0 , the electric field using $E_D/2$ where E_D is the Dreicer field, the momentum was normalized using mv_{th} , and the radial variable using the minor radius a . Figures 5, 6, and 7 present some of the results. It is observed that seed production has a strong dependence on t_* and T_M , but a weaker dependence on Z . Diffusion reduces the gradient of the radial seed density profile at the edge and this effect increases with the thermal quench time. RE seed production decreases when D_0 (normalized by 10^4 m²/s) increases and this effect is more noticeable near the edge. Finally, high momentum suppression of diffusive transport introduce momentum dependent production rate radial profiles. Further details can be found in [16, 17] and in a forthcoming publication.

VI. RUNAWAY DISSIPATION BY SECONDARY MATERIAL INJECTION IN ITER RELEVANT SCENARIOS USING THE RAMC CODE

Due to the potential difficulty of runaway electron (RE) avoidance in reactor scale tokamak plasmas, identifying robust means through which an existing RE beam can be terminated has emerged as a primary research thrust. The injection of large quantities of material into a RE beam results in a significant modification to both the phase space distribution of the RE population as well as to the bulk plasma. Understanding how these two components of the plasma evolve is critical to identifying effective RE termination schemes.

The RunAway electron Monte carlo (RAMc) code [9] has been utilized to describe the Ohmic to runaway electron (RE) current conversion during a tokamak disruption, along

with the subsequent decay of the RE beam due to material injection. Specifically, RAMc describes the phase space evolution of REs via a drift kinetic formulation while incorporating both small and large-angle collisions. This description thus allows for a kinetic treatment of the initial RE seed formation during the thermal quench, along with its subsequent amplification by the avalanche mechanism. The inductive electric field is evolved by a flux diffusion equation including both thermal and RE current components, which thus allows for the description of both an Ohmic to runaway conversion, along with the subsequent current plateau. In order to focus on these essential elements, the present formulation utilizes a simplified axisymmetric geometry. The present work thus complements other thrusts in the SCREAM project (led by KORC and CQL3D) focused on coupling runaway electron models to 3D MHD codes.

In the project, the phase space evolution of REs was evaluated for both low and high Z material injection for a prescribed temperature and charge state profile of the background plasma. Subsequently, the calculation was extended to incorporate a self-consistently evolved background plasma. Specifically, a power balance equation including radiative losses, Ohmic heating and energy transfer between the RE and thermal populations is used to evolve the electron temperature, whereas the charge state is evaluated from the screened hydrogen model FLYCHK [18]. The impact of low- Z material injection is illustrated in Fig. 8(a). Here a RE beam was formed via a rapid temperature quench of the plasma ($\tau_{TQ} = 0.25$ ms) leading to the formation of a RE seed via the hot tail mechanism. This seed is subsequently amplified by the avalanche mechanism leading to an Ohmic to RE conversion. At a time $t \approx 30$ ms a large amount of deuterium is injected into the runaway beam ($n_D = 40n_{D0}$). After this injection the plasma temperature is radiatively pinned to a value near $T_e \approx 1$ eV, which leads to the bulk plasma partially recombining. The momentum space evolution of the RE distribution in the presence of the cold, largely recombined plasma, is shown in Figs. 8(b) and 8(c). Here, the arrival of the injected deuterium leads to a small reduction in the average energy of the runaway population, a modest increase in the RE beam's average pitch, and a slight increase in the total number of runaway electrons. The origin of these modest changes to the RE beam's momentum space distribution despite the large increase in the RE dissipation is due to the inductive electric field increasing to a value comparable to the avalanche threshold, which is drastically increased by the material injection. Thus, while deuterium injection has a relatively modest impact on the momentum space profile of the RE beam, the current decay rate is significantly enhanced, as evident from Fig. 8(a).

VII. COUPLING NIMROD AND CQL3D TO STUDY RE GENERATION IN A DIII-D DISCHARGE

One-way coupling of NIMROD time evolved thermal quench MHD fields to the CQL3D Fokker-Planck runaway electron solver has been demonstrated. These early simulations examine a case with a modest level of runaway electron generation. The focus of this CQL3D study is on the effect of radial transport of the driven RE population due to the magnetic field fluctuations during the disruption, as taken directly from the MHD simulation

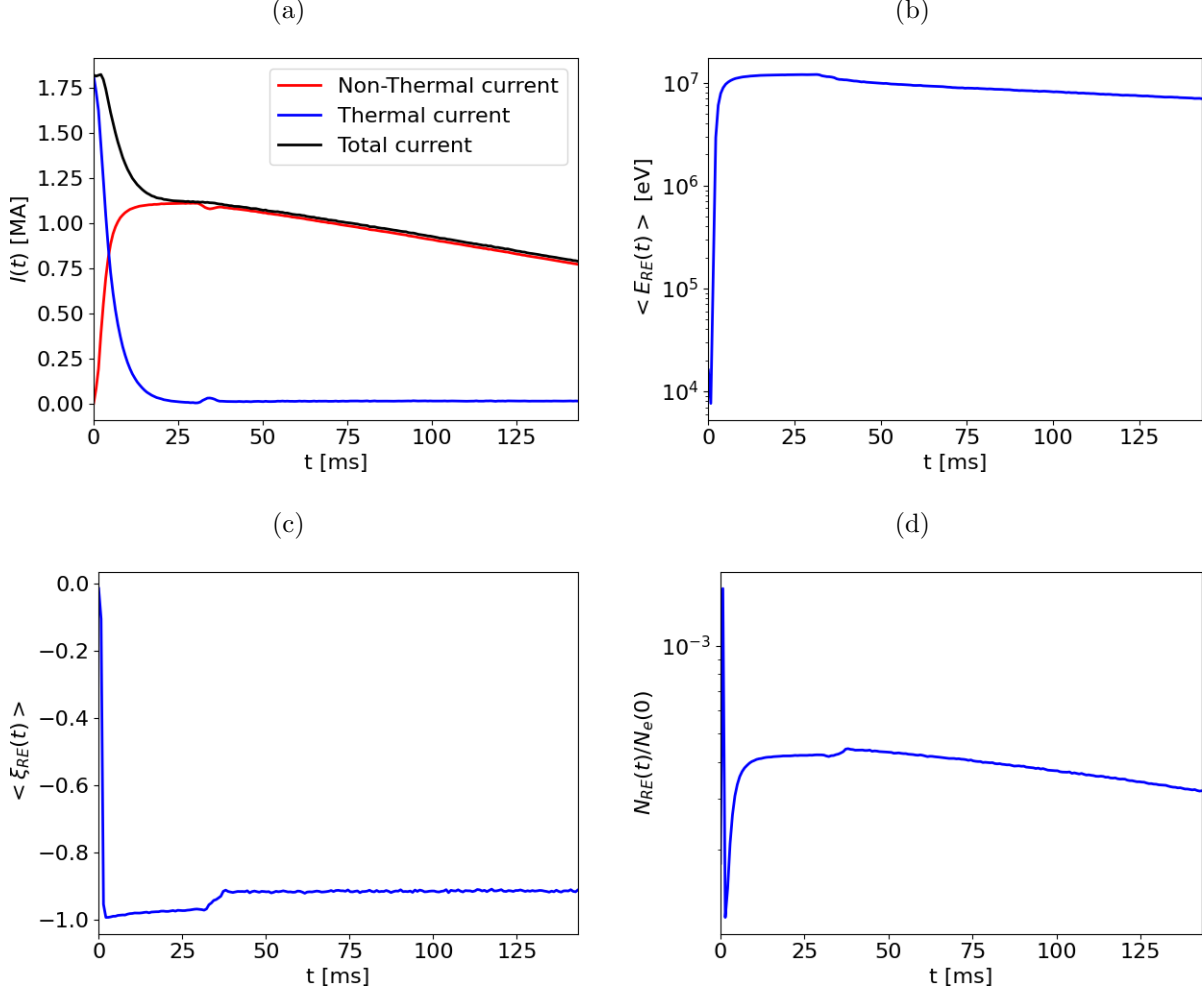


FIG. 8. (a) Net current evolution. The black curve indicates the total current, the red curve indicates the non-thermal current (i.e. runaway current), and the blue curve indicates the thermal current. (b) Average energy of the runaway distribution. (c) Average pitch of the runaway distribution. (d) Number of non-thermal electrons. A JET like case was assumed with roughly 1.8 MA of current initially present. A thermal quench with a time scale of $\tau_{TQ} \approx 0.25$ ms was imposed at the start of the simulation, where the temperature is evolved self-consistently after the thermal quench phase ($t \gtrsim 18$ ms).

of the DIII-D discharge discussed above.

The NIMROD Shattered Pellet Injection thermal quench simulation uses DIII-D equilibrium 160606 at 2990ms with 1.3MA of current and 0.7MJ of thermal energy. Figure 9 shows radiated power versus time and the total current and thermal energy versus time. The thermal quench occurs at $t=1.27$ ms and the current spike at $t=1.51$ ms. Figure 10 shows the outboard midplane profiles of temperature and total impurity density at $t=[0.0,0.5,1.0,1.235,1.335,1.475,1.8375]$ ms. Core temperature is maintained in the early part of the thermal quench ($t=[0.0,0.5,1.0]$ ms). The rapid drop in thermal energy and accompanying large peak in radiation are associated with the core collapse ($t=[1.235]$ ms). Impurities

mix into the core after the collapse of the core($t=[1.335,1.475,1.8375]$ ms). Poincare plots of figure 11 show the destruction of flux surfaces as the thermal quench proceeds. Several of these Poincare plots correspond to temperature and impurity density profiles shown in figure 10. Note that the flux surfaces begin to heal late in time once the thermal quench has completed and the current quench is underway.

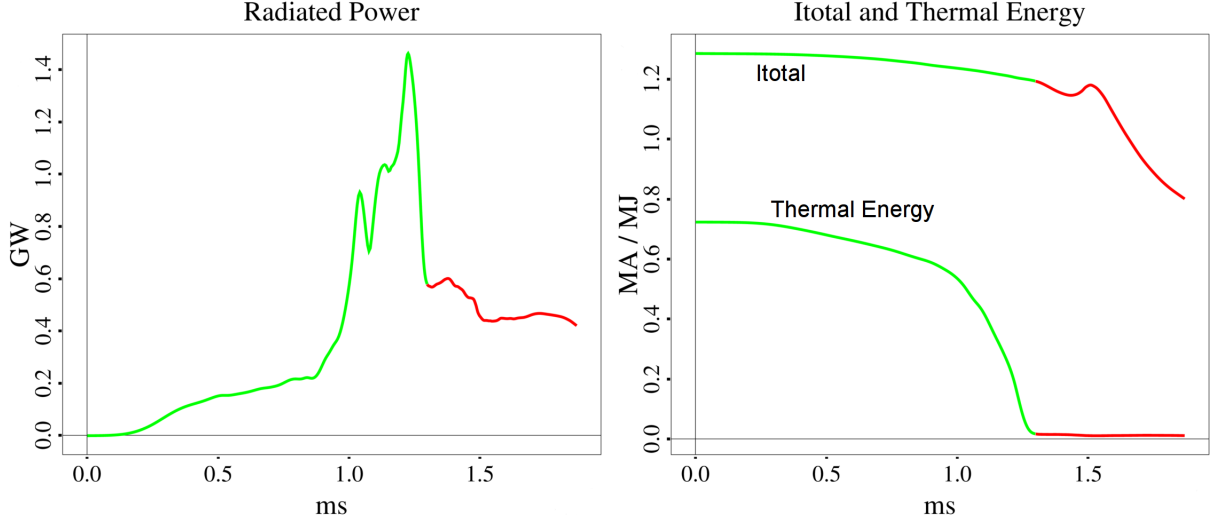


FIG. 9. Radiated power versus time and the total current I_{total} and thermal energy versus time. The thermal quench occurs at $t=1.27$ ms and the current spike at $t=1.51$ ms.

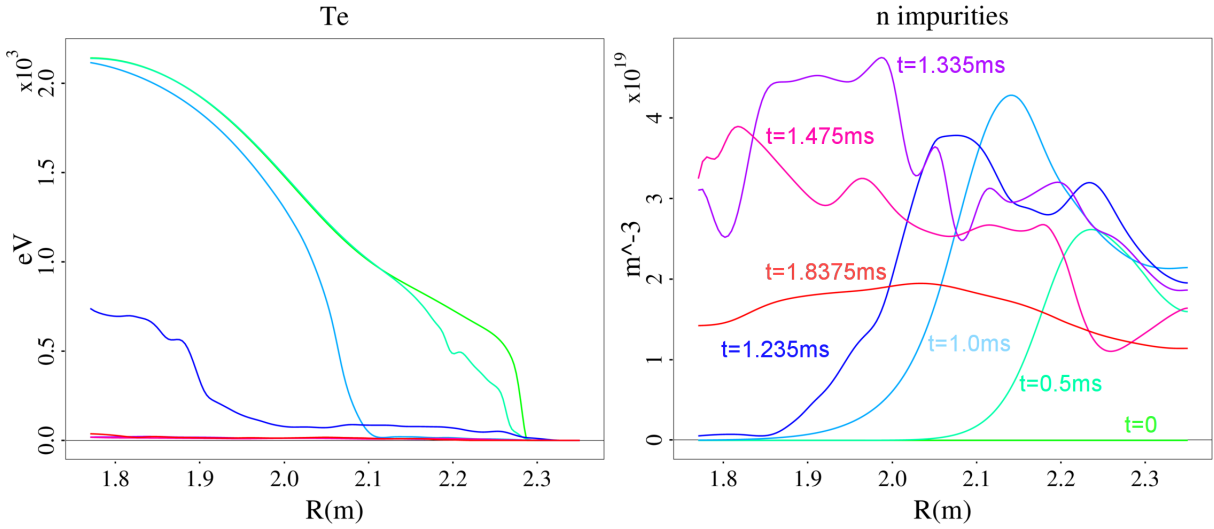


FIG. 10. Outboard midplane profiles of temperature and total impurity density at $t=[0.0,0.5,1.0,1.235,1.335,1.475,1.8375]$ ms.

The relativistic Collisional/QuasiLinear 3D toroidal geometry code CQL3D solves a Bounce-Averaged Fokker-Planck equation to obtain the 3 1/2-D distributions of electrons and multispecies ions, resulting from the balance between collisions, RF/neutral beam/particle sources, applied toroidal electric field, and radial diffusion. Steady-state and

time-dependent solutions are supported to create a general facility for the accurate calculation of heating and current drive in tokamaks. CQL3D provides a general model for the distortion of the electron and ion distribution functions resulting from auxiliary heating and current drive. The distributions are taken to be toroidally symmetric and independent of azimuthal angle about the ambient magnetic field.

Figure 12a from CQL3D (run without radial transport) shows that RE current reaches 0.7 MA during current quench phase (at $t > 1.65$ ms). As seen in 14a , the localization of RE current is mostly at $\rho \sim 0.8 - 0.9$, where the initial quick drop of temperature takes place (at $t = 0.5-1.0$ ms), and at $\rho < 0.4$, after the core temperature collapses (at $t \sim 1.65$ ms).

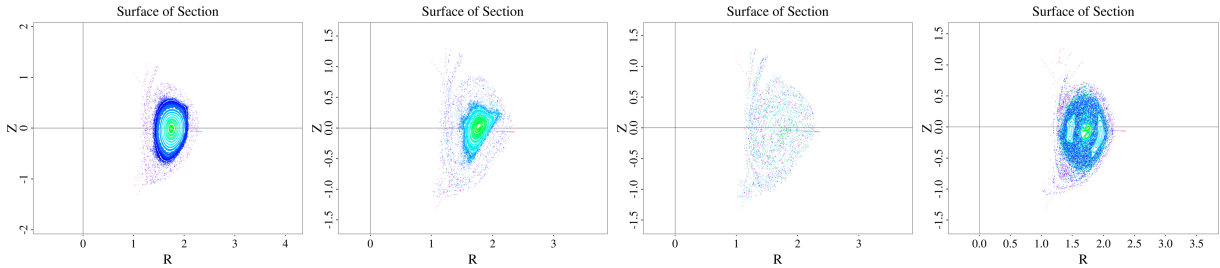


FIG. 11. Poincaré plots corresponding to profiles in figures 2 show destruction of flux surfaces through the thermal quench and healing late in time.

For greater compatibility with the CQL3D model a more complete neoclassical Spitzer resistivity has been implemented into the NIMROD code. This resistivity computes the explicit Coulomb Logs, includes evolving Z_{eff} taking into account the ionizing/recombining charged states of impurities, and includes the Sauter trapped electron correction [19].

Figure 13 from CQL3D shows the distribution at two radii where a large fraction of RE was computed, as shown in Fig.14a. Both distributions in Fig. 13 are shown at 2ms in the simulation. For $\rho = 0.795$, the bump-on-tail is clearly visible at $p/mc = 3$ (which is

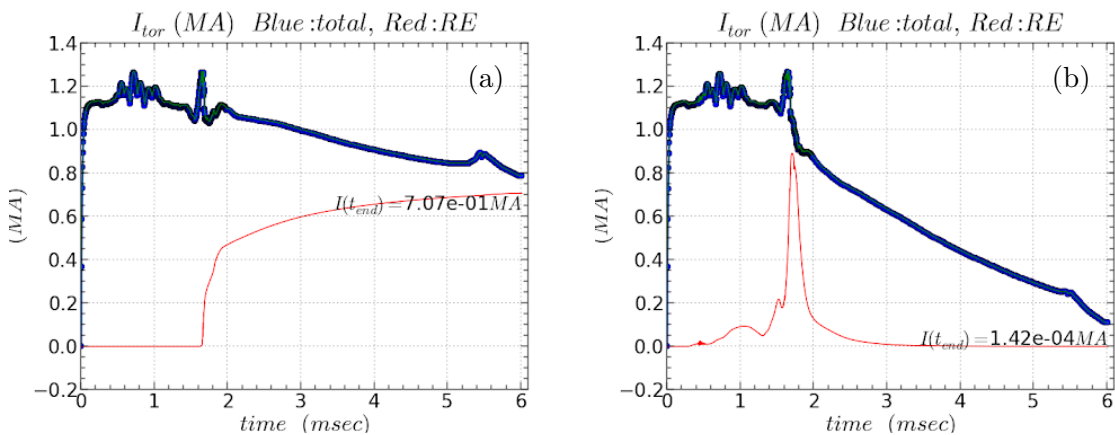


FIG. 12. Total (bold/blue) and RE (red) current computed with CQL3D based on NIMROD SPI MHD fields – (a) without radial transport, and (b) with $\delta B/B$ radial transport. Thermal quench takes place at $t \sim 1.60 - 1.65$ ms.

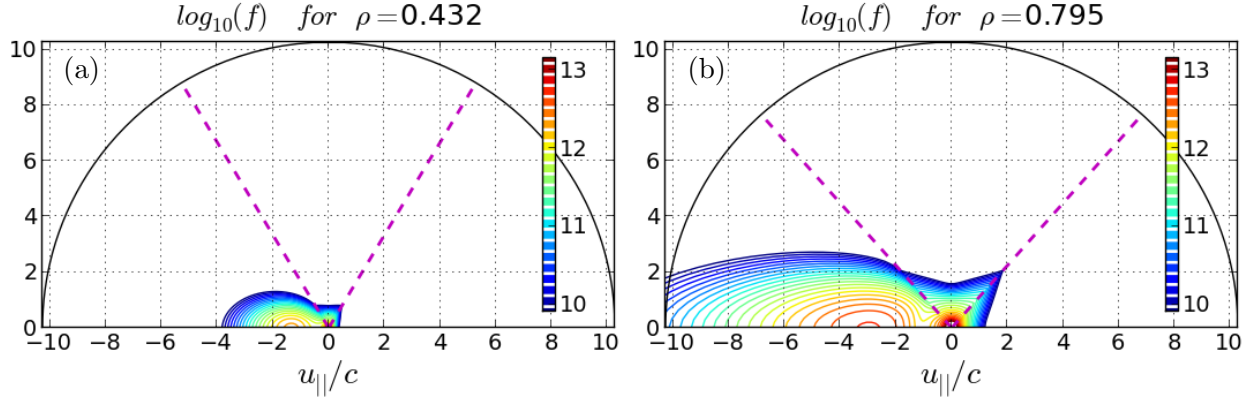


FIG. 13. Distribution functions from CQL3D at two radial locations, $\rho = 0.432$ (a) and $\rho = 0.795$ (b), both at 2ms in the simulation shown in Fig. 14a.

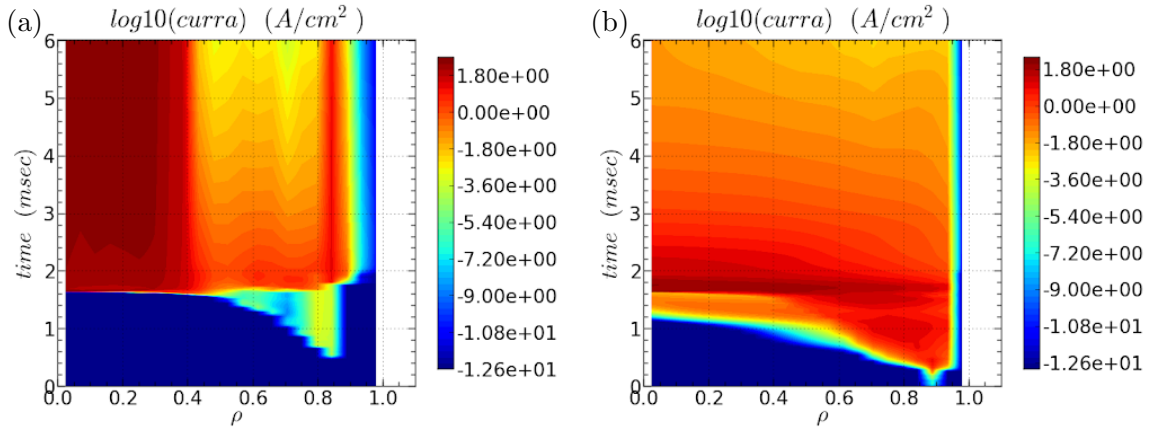


FIG. 14. RE current density $J_{RE}(\rho, t)$ in \log_{10} scale computed with CQL3D – (a) without radial transport, and (b) with $\delta B/B$ radial transport. Thermal quench takes place at $t = 1.60$ - 1.65 ms.

1.1 MeV). Under the influence of the positive toroidal electric field, the bumps continue to evolve towards higher energies. The bump-on-tail also suggests possible microinstability, and this will be further examined in conjunction with the GENRAY ray tracing code.

Subsequently, an investigation was begun into the effects of electron radial transport caused by magnetic field fluctuations. The CQL3D internal model for radial transport was upgraded to accept the time-dependent data for $\delta B(\rho, t)/B(\rho, t)$ from NIMROD, and to form the radial diffusion coefficients $D_{rr}(\rho, t)$ based on an existing analytic model [20, 21].

When the $\delta B/B$ transport is included into CQL3D simulations, the RE current drops to a very small level of 140 A, as seen in figure 12b. Interestingly, the RE current briefly becomes larger (at $t < 1.7$ ms) than without the radial transport. This effect is under investigation. With the radial transport enabled, the RE current is less localized in radius at $t > 1.65$ ms, as seen from Figure 14, however, at pre-TQ time range the “precursor” RE current emerges locally at $\rho \sim 0.7 - 0.9$.

Note that little RE was observed in the experimental discharge being modeled, and not a

large RE population resulted from the modeling when radial transport is enabled. It should be noted that according to NIMROD data, the magnitude of $\delta B/B$ briefly reaches large values of 0.05 (5%) during TQ phase ($t \sim 1.6 - 1.7$ ms). In CQL3D run presented in figures 12 and 14, the data on $\delta B/B$ was scaled down by factor of 32, effectively reducing the radial diffusion coefficient by factor of 1000. The runs with the original levels of $\delta B/B$ turned out to be unstable for the particular run mode being used in CQL3D. This run will be further investigated, particularly with two-way coupling of NIMROD and CQL3D, which is under development. However, given the small number and current of REs, the one-way coupling is sufficient, and not much difference is expected from the result with two-way modeling in this case.

VIII. RUNAWAY MITIGATION, TRANSPORT AND SYNCHROTRON MODELING USING KORC

This section discusses results using the Kinetic Orbit Runaway electrons Code (KORC) to better understand DIII-D and JET experiments of RE mitigation via secondary impurity injection, initial coupling to the extended-MHD codes NIMROD and M3D-C1, and improvements of its synchrotron emission synthetic diagnostic. The work simulating experiments provides a necessary validation of physical models and yields insight to experimental results, while the initial coupling with extended-MHD codes sets the foundation for more sophisticated couplings to be developed.

A. KORC modeling of RE mitigation using high-Z impurity injection

KORC is extended to model post-disruption runaway electron (RE) mitigation by impurity injection [22]. KORC was used to study RE mitigation by secondary impurity injection into the post-disruption RE plateau beam of DIII-D discharge 164409 with Ne MGI and JET pulse 95128 with Ar SPI. Guiding center RE orbits are calculated by interpolating experimental fields and plasma profile information. Time-sequenced magnetic reconstructions are generated using JFIT for DIII-D and EFIT for JET, where magnetic flux contours are shown in the rightmost plots of Fig. 15 with DIII-D in the top row and JET in the bottom row. The inductive toroidal electric field is calculated from the time-derivative of the flux calculated using JFIT and EFIT reconstructions and agrees well with experimental loop voltage measurements, except during a vertical displacement event (VDE) in JET 95128 (not shown).

An analytic model is employed for electron and impurity densities, where free parameters are fit by using a synthetic line-integrated density diagnostic to compare directly with experimental data. The fit between model and experiment is shown in the leftmost plots of Fig. 15 where the solid traces are from the experiment and the dashed lines are from the model. Additionally, simple model profiles are used for including neutral impurities, where a constant and uniform profile is used in the results presented here. These profiles are used in a Fokker-Planck linearized Coulomb collision operator that is implemented as

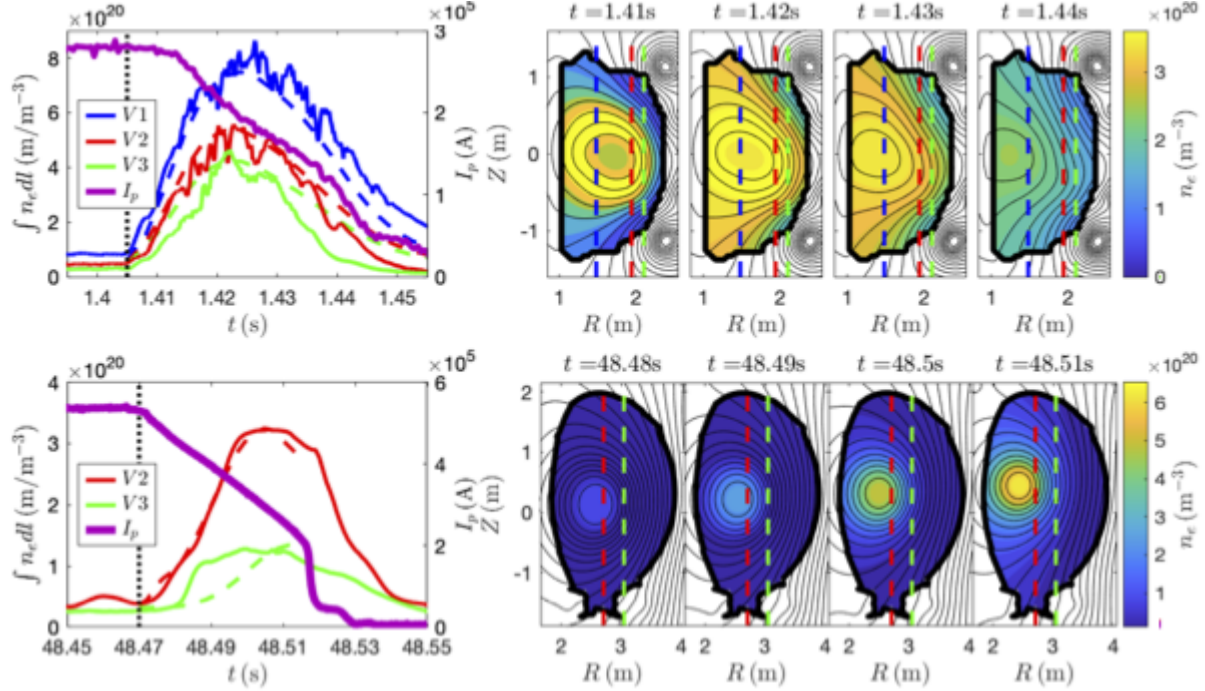


FIG. 15. Top row corresponds to DIII-D 164409 with Ne MGI and bottom row to JET 95128 with Ar SPI. Solid traces in the left plots show experimental plasma current and line integrated density (LID) and dashed traces show synthetic LID of the model used in KORC calculations. The right plots show the evolution of the model electron density profile that corresponds to the synthetic LID displayed in the left plots overlaid with black contours of instantaneous poloidal flux.

stochastic differential equations for 2D phase-space momentum to evolve degrees of freedom for each RE. Transport coefficients include the physics of partially-ionized impurities [23], including neutral impurities. Lastly, synchrotron and bremsstrahlung radiation are included within the algorithm for evolving the GC equations of motion, which play a minor role in RE mitigation.

Results of KORC calculations are shown in Fig. 16. The solid black and green traces in the top plots of Fig. 16 indicate the normalized RE current and energy, respectively, calculated by KORC, where the dotted black trace indicates the normalized experimental current. The red and blue traces indicate the fraction of deconfined and thermalized RE, respectively, where a RE is thermalized when its momentum drops below m_{ec} . The simulations for DIII-D 164409 demonstrate that RE deconfinement losses during plasma scrape off is the primary current reduction mechanism in DIII-D experiments with high-Z impurity injection, and not collisional slowing down. The bottom plots in Fig. 16 show the simulated RE power flux deposited into the inner wall limiter. RE power flux is calculated by scaling each RE's energy by the ratio of the initial KORC and experimental RE current. Because the magnetic configuration is assumed axisymmetric, so is the RE deposition (not shown). The maximum total power deposited on the inner wall is approximately a factor of 5 larger for JET than DIII-D (not shown). The wall deposition pattern is qualitatively different in the two cases;

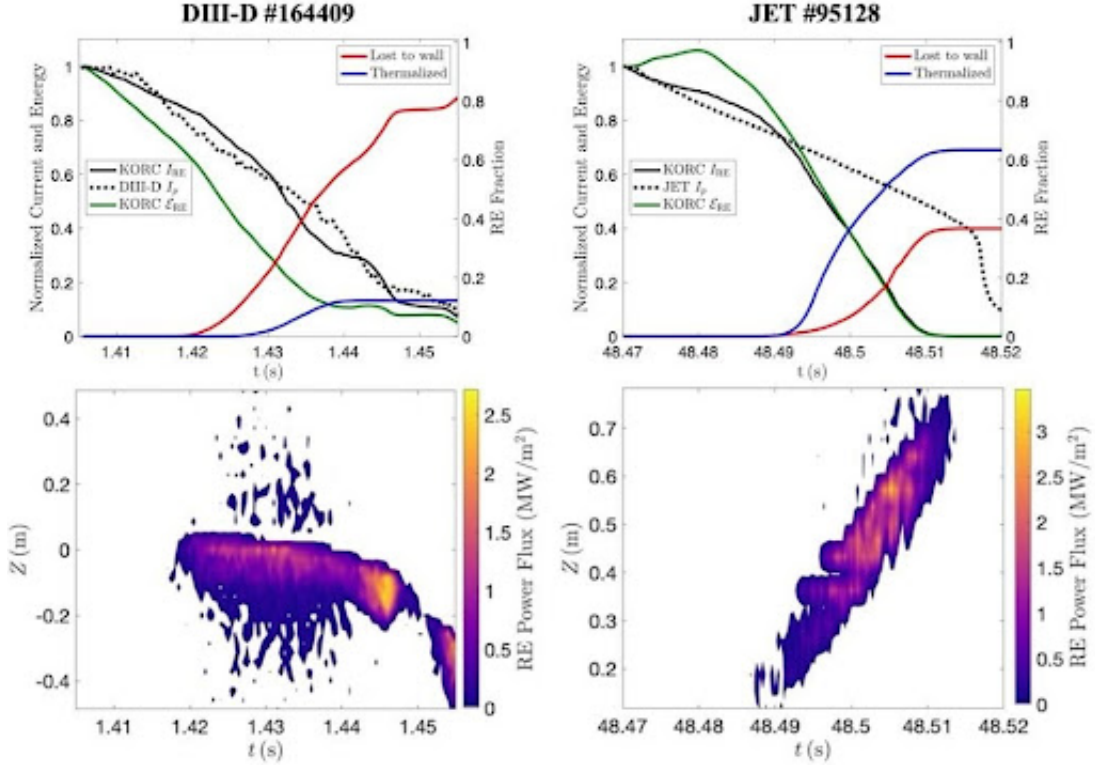


FIG. 16. Comparison of evolving RE current (solid black trace), energy (green trace), deconfinement (red trace), and thermalization (blue trace) calculated by KORC in the top row of plots for DIII-D 164409 (left plot) and JET 95128 (right plot). The experimental current is shown for each case by the dotted black trace. The RE power flux deposited on the inner wall as a function of time is shown in the second row of plots for each simulated case.

DIII-D 164409 had the RE beam advect toward the wall due to less effective horizontal position control at low current, while JET 95128 advects inward and upward toward the wall while beginning to undergo a VDE. This upward advection increases the total area over which REs deposit their energy and may prove beneficial. While the KORC simulations agree well throughout the RE mitigation phase in DIII-D 164409, there is less agreement in the latter part of the RE mitigation phase in JET 95128. We posit that the uncertainty in the neutral impurity transport, and in general, the plasma and partially-ionized impurity transport, is also having an effect. Improved neutral transport modeling will be addressed in future work by coupling KORC to the 1D plasma and impurity transport model in Ref. [24].

Figure 17 explores the subtle balance between the evolution of the magnetic configuration, loss of confinement, and collisions. The spatiotemporal plots in this figure show the time evolution of the normalized density of RE as function of the major radius R . Consistent with the time evolution of the REs lost to the wall shown in the red curve of the top left plot Fig. 16, a depletion of the beam density is observed as function of time. But, most importantly, these plots provide interesting information about the spatial location where the beam is lost. Panels (a), (c) and (d) show the evolution for different energies in the presence

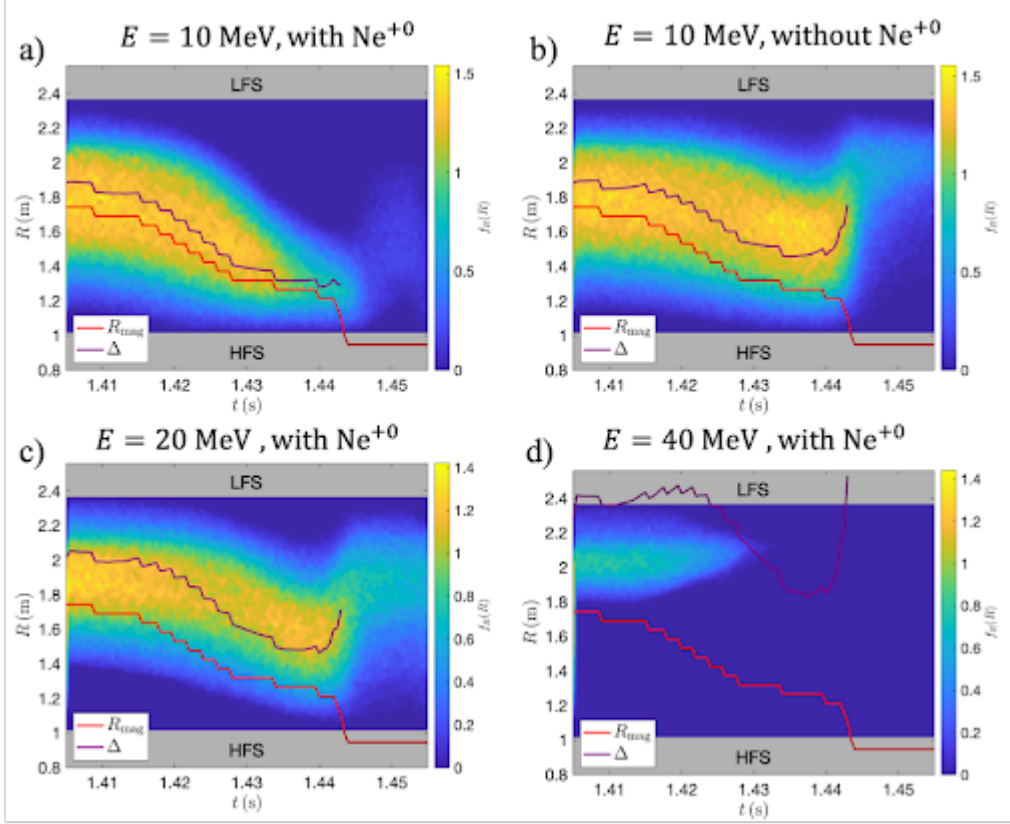


FIG. 17. Spatiotemporal evolution of radial density of RE with and without Ne^{+0} impurities for different initial energies. Shown also are the time evolution of the magnetic axis (red traces) which is consistent with Fig. 17 drifts towards the HFS (high field side), and the drift estimate of the RE beam center, Δ (purple traces), which depending on the energy and the impurities can drift towards the HFS or the LFS (low field side).

of Ne^{+0} impurities, and panel (b) shows a case in the absence of Ne^{+0} impurities. The significant role of the impurities is observed in panels (a) and (b) that follow the evolution of a 10 MeV beam. In the presence of Ne^{+0} impurities the RE beam drifts towards the high field side (HFS), but in the absence of Ne^{+0} impurities this drift is arrested by an eventual migration of the RE beam towards the low field side (LFS).

The main two effects contributing to the radial displacement of the RE beam are the drift of the magnetic field axis, R_{mag} , towards the HFS (shown in Fig. 16 and tracked with red lines in Fig. 17), and the drift of orbits of the RE, whose centre Δ is tracked in the purple lines in Fig. 17. In the absence of impurities, panel (b), the energy dissipation is minimal, and the LFS drift of Δ (which increases with energy) can compensate the HFS drift of the magnetic axis. However, as shown in panel (a), adding impurities reduce the energy and the LFS drift of Δ . Consistent with this picture, increasing the initial energy of the RE beam, enhances the LFS drift of Δ , and as shown in panel (d) leads to a net drift towards the LFS. Finally, comparing cases (b) and (c), it is interesting to note that an increasing the energy and the impurities have a similar qualitative effect as decreasing both.

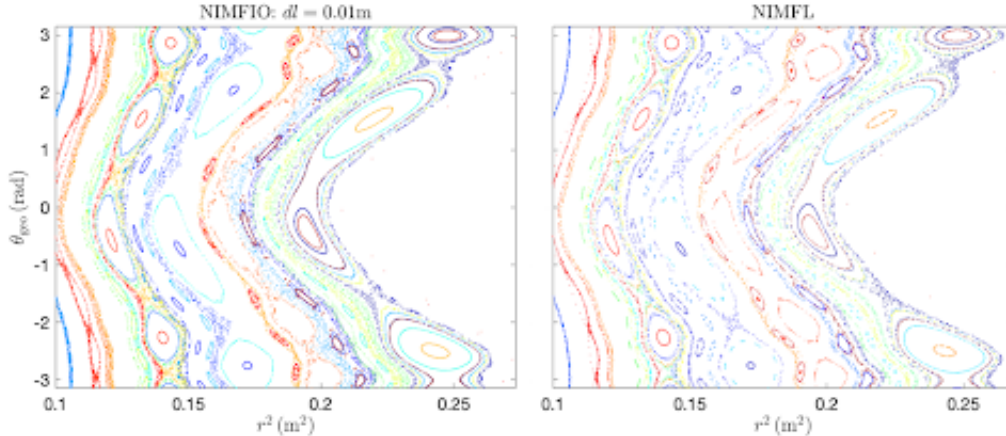


FIG. 18. Poincaré sections using Fusion-IO interpolation of NIMROD fields NIMFIO (left) and native NIMROD NIMFL (right).

B. Coupling KORC with extended-MHD codes

A one-way coupling of KORC with the M3D-C1 and NIMROD extended-MHD codes has been developed using the Fusion-IO application programming interface (API) [25]. The present capabilities allow tracer RE orbits to be simulated using non-axisymmetric magnetic and electric fields, field gradients, and plasma and impurity profiles interpolated from the native spatial representation of extended-MHD calculations. As a first step to understand the role of magnetic field stochasticity on the confinement of RE, in [26] we performed a numerical study of the dependence of orbit effects on the size and degree of overlap of magnetic islands.

The one-way coupling with MHD codes was verified by comparisons of Poincaré sections generated by Fusion-IO interpolation and from Poincaré modules native to each extended-MHD code. The results for a NIMROD test case are shown in Fig. 18. We find good qualitative agreement between the two methods and comment that the quantitative differences are most likely due to the different algorithms for field line tracing and interpolation at the location of the section crossings.

1. KORC coupling with NIMROD

The developed one-way coupling between KORC and NIMROD using Fusion-IO [27] has been used to evolve the RE distribution in visco-resistive NIMROD simulations of RE deconfinement by resonant magnetic perturbation (RMP) application in the Madison Symmetric Torus (MST) assuming cold ions [28, 29]. Experiments find that while $m = 3$ RMPs deconfine REs generated in low-density tokamak discharges, $m = 1$ RMPs do not significantly deconfine REs. NIMROD simulations of these discharges show sawtooth activity and a stochastic edge region with RMPs applied, where the $m = 3$ RMPs result in a wider stochastic region compared to $m=1$ RMPs. The confinement difference is qualita-

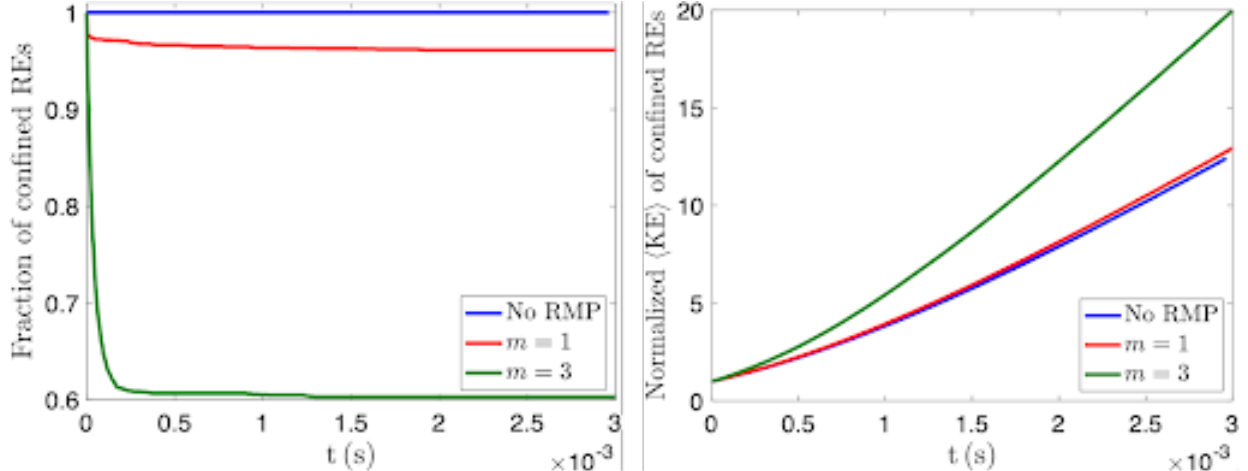


FIG. 19. One-way coupling of KORC and NIMROD simulations of RMP application on MST. The left plot shows that $m = 3$ RMPs deconfine a significant fraction of REs over a sawtooth cycle, while $m = 1$ RMPs do not lead to any significant deconfinement. The electric field doesn't affect the confinement over a single sawtooth cycle, but the right plot shows that the average energy of confined REs increases more rapidly in the $m = 3$ case.

tively found in KORC simulations of multiple sawtooth cycles shown in Fig. 19, where full orbits are evolved beginning with a 30 keV monoenergy and 10° monopitch RE beam that is uniformly distributed within the normalized poloidal flux surface of $\psi_N = 0.9$. The left plot indicates that after approximately 3% immediate losses, the $m = 1$ RMP case (red trace) confines nearly all REs while the $m = 3$ RMP case (green trace) has nearly 40% of REs deconfined. The majority of deconfined REs are from the stochastic edge region (not shown), and the sawtooth cycle appears to play a minor role in these calculations. It was hypothesized that the stochastic region and sawteeth work synergistically to deconfine REs over several sawtooth cycles completely, however, this is not observed in present simulations. The right plot of Fig. 19 shows the average energy of the confined REs is increased at a significantly faster rate with the $m = 3$ RMP, compared to the $m = 1$ and without cases. As the average energy continues to increase, drift orbit effects would also increase and lead to additional deconfinement. However, present calculations indicate this happens on a longer time scale than observed experimentally. Additional NIMROD simulations will explore how electric field acceleration changes as visco-resistive effects are varied and thermal ions are included.

2. KORC coupling with M3D-C1

This one-way coupling between KORC and M3D-C1 using Fusion-IO has been used to evolve RE distributions in M3D-C1 simulations of DIII-D discharge 160606 with Ne pellet-induced disruptions for controlled shutdown scenarios on DIII-D [30]. We note that DIII-D discharge 160606 does not result in a post-disruption RE beam. The plasma and impurity

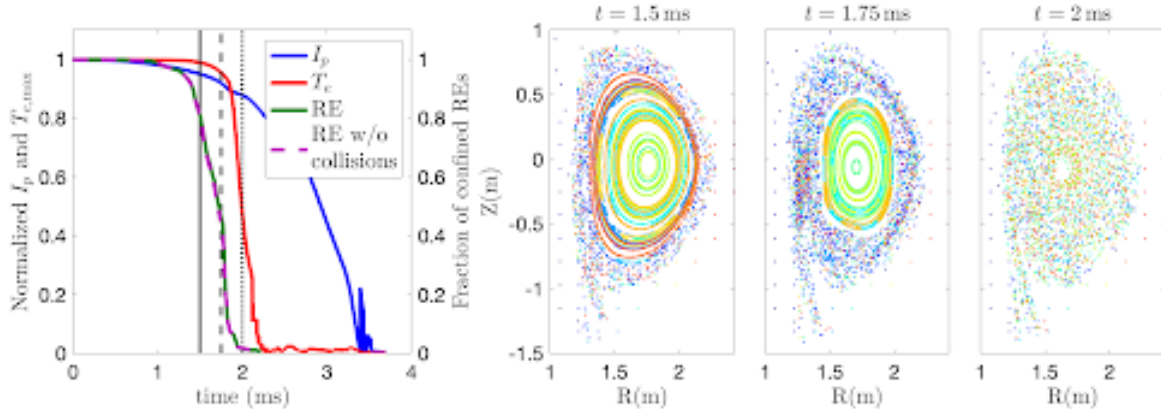


FIG. 20. One-way coupling of KORC and M3D-C1 simulation of Ne SPI into DIII-D. Simulated evolution of plasma current and maximum electron temperature from M3D-C1 and fraction of confined RE from KORC with and without collisions (left plot). Poincaré sections of M3D-C1 calculated magnetic field during TQ (right plots), where the vertical lines in the left plot indicate the times in the right plots.

details are used to evaluate linearized Coulomb collision operators and, because M3D-C1 evolves all charge states of a given impurity using the KPRAD model [31], the effects of partially-ionized impurities [23] are included. KORC calculates guiding center RE orbits starting from a 10 MeV monoenergy and 10° monopitch beam uniformly distributed within the last closed flux surface.

Figure 20 shows the resulting evolution during the simulated disruption. The left plot indicates the evolution of the M3D-C1 calculated plasma current (blue trace) and electron temperature (red trace), KORC calculated fraction of confined REs with (green trace) and without (dashed violet trace) collisional effects included, and the vertical lines indicate the times corresponding to the Poincaré plots to the right. The KORC simulation shows that all REs are deconfined during the thermal quench on a faster time scale than the thermal energy loss. The macroscopic evolution of the normalized RE current is qualitatively the same in both collisional and collisionless simulations, indicating that confinement losses are the dominant physical process for seed REs during the current quench. The complete loss of REs is consistent with the experimental observation of no post-disruption RE beam. We note that closed flux surfaces are reformed later during the current quench. Future studies will look at KORC simulations of RE generation during this phase using solution fields from M3D-C1 using a fluid-RE species.

Figure 21 shows the evolution of the confinement of the collisional simulation, indicating the spatial distribution at time times indicated by the vertical lines in Fig. 20. As the MHD mode calculated by M3D-C1 grows (not shown), the magnetic configuration gets increasingly stochastic, and fewer REs (colormap) are confined. Additionally, the area wetted by deconfined REs (red locations) is in the lower divertor region and increases as the MHD mode grows. We note that the collisionless simulation exhibits qualitatively similar behavior. The growth of the MHD mode has a strong effect on the axisymmetry of the wetted

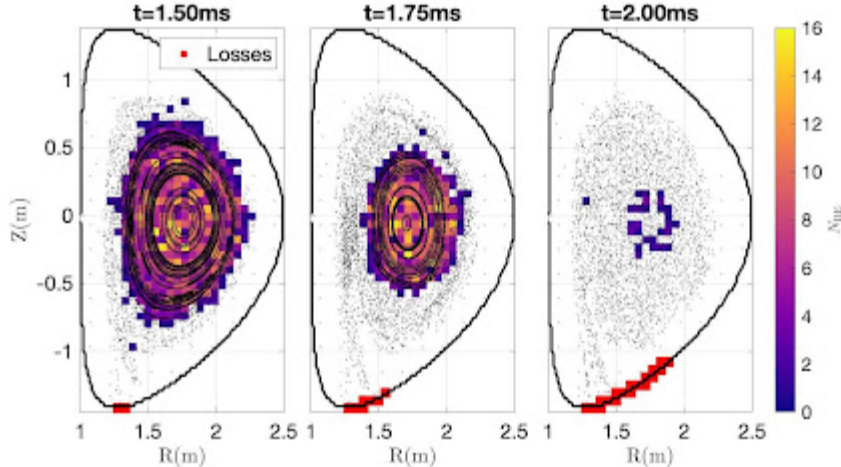


FIG. 21. Distribution of confined (colormap) and location of deconfined (red locations) REs as the magnetic field from M3D-C1 simulations becomes increasingly stochastic.

area (not shown). Initially, when the MHD mode is of small amplitude, REs are deconfined axisymmetrically. When the MHD mode grows, the wetted area spirals out as the magnetic configuration becomes increasingly nonaxisymmetric. Again, we note that the collisional simulation exhibits qualitatively similar behavior.

While the effects of collisions are not borne out in the macroscopic evolution due to the dominance of deconfinement effects, they are indeed finite. Using approximate plasma and impurity values at an intermediate time in the simulations (1ms), $n_e = n_i = 3.6 \times 10^{20} \text{m}^{-3}$, $T_e = 2 \text{keV}$, $n_{\text{Ne,max}} = 4.9 \times 10^{19} \text{m}^{-3}$, $Z_{\text{eff,max}} = 7.9$, for a 10MeV RE the pitch angle scattering time scale is $\tau_D = 0.14 \text{s}$ and the slowing down time scale is $\tau_S = 55 \text{ms}$. These collisional time scales are much longer than the 1ms time for RE deconfinement, consistent with collisions playing a small role in the macroscopic evolution. To observe the effects of collisions in these simulations, we need to look at the evolution of the distribution functions, as shown in Fig. 22. The evolution of the pitch angle distribution is shown in the left column of plots, where collisions broaden out the profile compared to the collisionless case. The collisionless case does exhibit some pitch angle scattering, as described in Ref. [5]. The evolution of the momentum distribution is shown in the right column of plots, where electric field acceleration plays the dominant role in increasing the average energy of the ensemble. The effects of collisions can be observed to slow the acceleration due to the electric field marginally.

C. Synchrotron modeling with KORC

Synthetic diagnostics are essential for model validation. Based on our early work [32], we developed and implemented more efficient and accurate algorithms for the computation of synchrotron emission (SE). For toroidally symmetric systems, the new version of KORC's synthetic diagnostic uses a faster and more accurate numerical method that conserves exactly

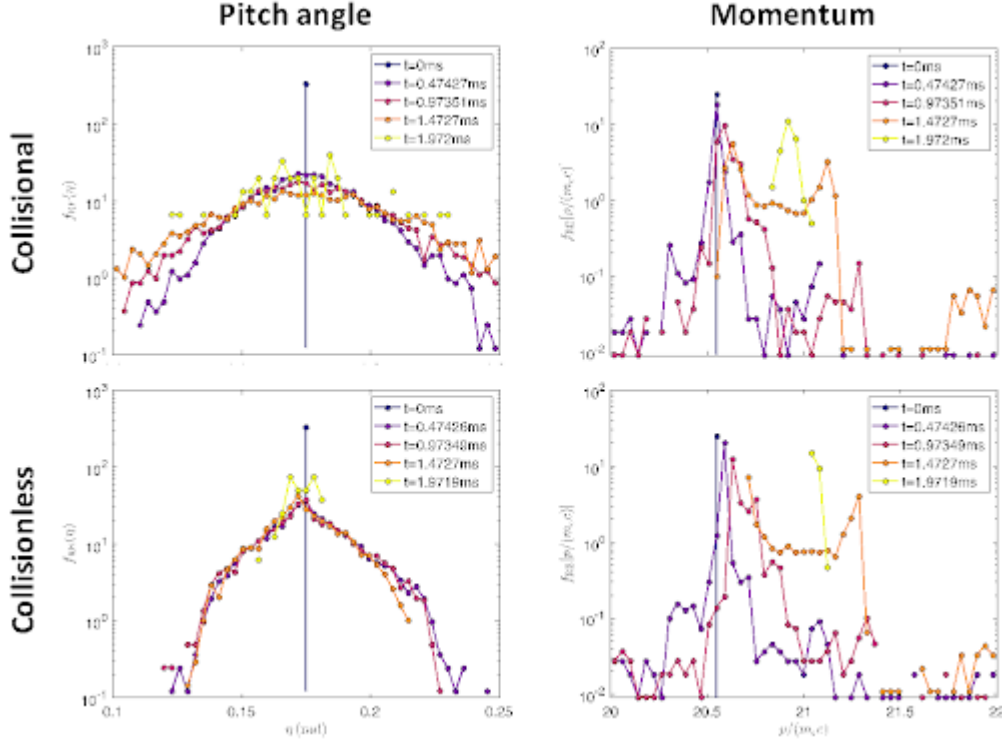


FIG. 22. Evolution of the distribution of pitch angle (left column) and momentum (right column) for collisional (top row) and collisionless (bottom row) KORC simulations.

the angular momentum and uses the symmetry to increase the efficiency of the Monte Carlo sampling. Of particular interest was the incorporation of the SE polarization physics.

In the recently published paper [33] we applied the extended synthetic diagnostic to SE polarization measurements in DIII-D. The main focus was the study of the dependence of the vertical and horizontal polarization ratio, P_Z/P_X , on the pitch angle of the runaway electrons. Visible images from fast-framing cameras with a linear polarizer were analyzed and showed that the RE plateau synchrotron emission is predominantly linearly polarized along the vertical direction. Consistent with KORC's synthetic diagnostic results, the image-average intensity ratio P_Z/P_X was measured to be between 3 and 14, with a mean polarization ratio, $\langle P_Z \rangle / \langle P_X \rangle \sim 6$. In addition, as Fig. 23 shows, both the crescent shape unpolarized images and the up-down asymmetric horizontally-polarized images are in qualitative agreement.

We also used KORC to study the dependence of the polarization ration, P_Z/P_X , on the pitch angle. As shown in Fig. 24 a monotonically increasing dependence was observed. The sensitivity of P_Z/P_X , on the pitch angle opens the possibility of using this ratio to experimentally infer the pitch angle. We have also benchmark KORC with the European code SOFT. As Fig. 24 shows, there is good qualitative agreement. However, the polarization ratios are systematically higher in SOFT than in KORC. This might be due to the fact that whereas KORC incorporates full orbit and full angle radiation dependences, SOFT uses the guiding center and the radiation cone model approximations. There might be also potential

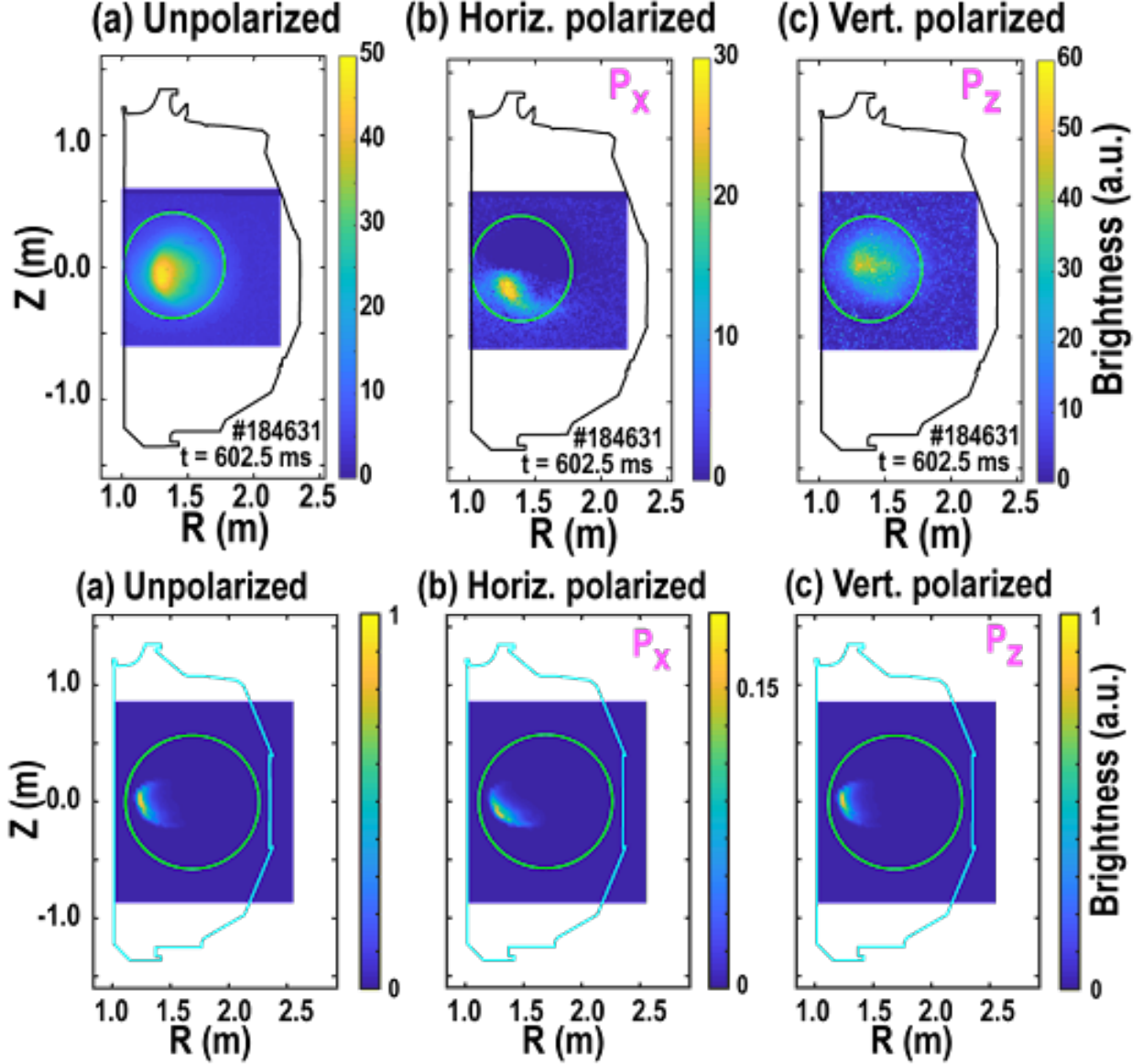


FIG. 23. Synchrotron emission (SE) from RE beam: (a) unpolarized, (b) horizontally and (c) vertically polarized brightness. The top row shows the experimentally measure brightness and the bottom panel the generated camera images (normalized to the magnitude of the brightness of the unpolarized image) using KORC synthetic diagnostic. In agreement with the experiment, the computations show a mean polarization ratio, $\langle P_Z \rangle / \langle P_X \rangle \sim 6$. Adapted from [33].

differences in the details regarding the implementation of the initial conditions, and the role of transients that can lead to the rapid loss of confinement and collisionless pitch angle dispersion, captured in KORC but not in SOFT.

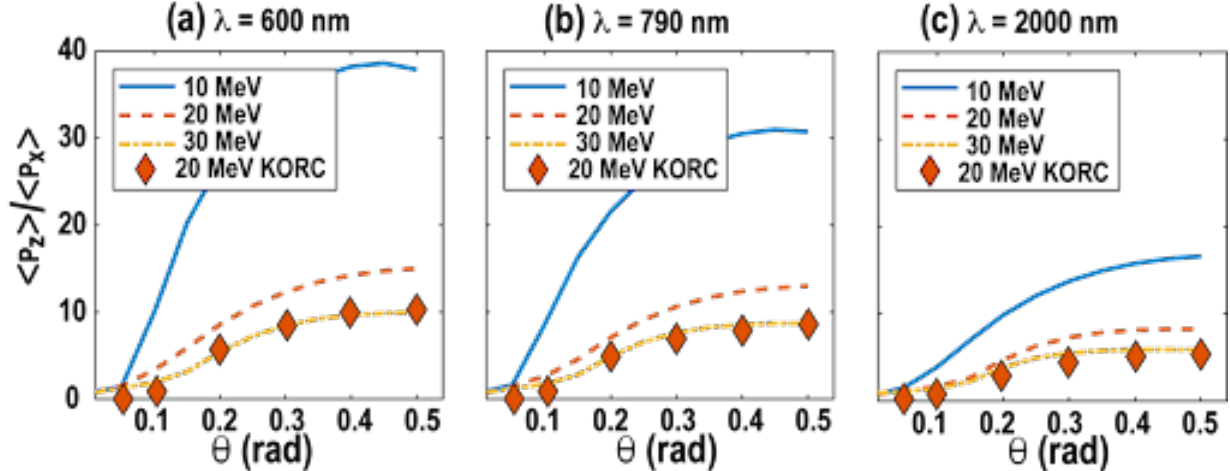


FIG. 24. Comparison of the spatially averaged polarization ratio vs. pitch angle calculated using SOFT (lines) and KORC (symbols) for several mono-energetic distributions. Imaging wavelengths simulated are (a) 600 nm, (b) 790 nm, and (c) 2000 nm. . Adapted from [33].

IX. SUMMARY

In the initial stages of this project, there was a focus on specific experiments in DIII-D [12] where disruptions were induced with impurity injection. Under the prescribed conditions, the experiment was generally without runaway generation. This offered the ability to validate, at least in a broad sense, several codes on the prediction of the threshold for substantial runaway seed generation and to explain the physical processes responsible for the lack of runaways observed in the experiment.

An interesting point realized from this work is that the initial magnitude and rate of collapse of temperature, and the radial transport of runaways due to 3D magnetic field perturbations, simultaneously contributed to the observed outcome of a lack of driven runaways in experiment. Further work with the capabilities developed in this project will provide more insight into the relative importance of these two processes in various scenarios.

Subsequent analysis has focused on DIII-D and JET discharges, and ITER relevant simulations, exhibiting significant runaway electron generation. Overall, several other aspects of runaway seed generation, and the subsequent dissipation, were studied in a general sense, and with a focus on specific experiments. More details of these results from the whole project will subsequently appear in journal publications.

One of the greatest technical challenges remaining to quantitatively predict the runaway generation in experiment is in the coupling of runaway current calculated in kinetic codes such as CQL3D and KORC back into the MHD simulation codes such as M3D-C1 and NIMROD. In this report, a one-way coupling has been shown, which is sufficient for low runaway current applications. Achieving this capability will allow the quantitative prediction of runaway seed confinement in high current, fast disruptions, which can carry the highest risk. This development would also bring us one step closer to a whole device model for magnetic confinement fusion.

The great many code developments that were achieved for this project will have positive impact on the ability to conduct scientific research, even extending beyond runaway electron modeling and disruptions, for years to come. From the effort reported here we're now more confident in our understanding of the extent to which each physics mechanism studied would be important in a variety of scenarios. We are now developing the capability to routinely and accurately simulate runaway generation through a thermal collapse, which has allowed, and will continue to allow, for the realistic exploration of avoidance and mitigation techniques.

-
- [1] G. Zhang and D. del Castillo-Negrete, “A backward Monte-Carlo method for time-dependent runaway electron simulations”, *Phys. Plasmas* **24**, 092511 (2017).
 - [2] K. Huang, I. Gamba, and M. Abelmalik, “CCPWRS: A Conservative code for Collisional Particle-Wave Resonance System”, In preparation (2021).
 - [3] R. Harvey, V. Chan, S. Chiu, T. Evans, M. Rosenbluth, and D. Whyte, “Runaway electron production in DIII-D killer pellet experiments, calculated with the CQL3D/KPRAD model”, *Physics of Plasmas* **7**, 4590 (2000).
 - [4] D. Daniel, W. Taitano, and L. Chacón, *Comput. Phys. Comm.* **254**, 107361 (2020).
 - [5] L. Carbajal, D. del Castillo-Negrete, D. Spong, S. Seal, and L. Baylor, “Space dependent, full orbit effects on runaway electron dynamics in tokamak plasmas”, *Physics of Plasmas* **24**, 042512 (2017), <https://doi.org/10.1063/1.4981209>.
 - [6] C. R. Sovinec, A. H. Glasser, T. A. Gianakon, *et al.*, *J. Comp. Phys.* **195**, 355 (2004).
 - [7] A. Stahl, M. Landreman, O. Embréus, and T. Fülöp, “NORSE: A solver for the relativistic non-linear Fokker-Planck equation for electrons in a homogeneous plasma”, *Computer Physics Communications* **212**, 269 (2017).
 - [8] N. Ferraro, B. Lyons, C. Kim, Y. Liu, and S. Jardin, “3D two-temperature magnetohydrodynamic modeling of fast thermal quenches due to injected impurities in tokamaks”, *Nucl. Fusion* **59**, 016001 (2018).
 - [9] C. McDevitt and X.-Z. Tang, “Runaway electron generation in axisymmetric tokamak geometry”, *EPL (Europhysics Letters)* **127**, 45001 (2019).
 - [10] B. N. Breizman, P. Aleynikov, E. M. Hollmann, and M. Lehnen, “Physics of runaway electrons in tokamaks”, *Nuclear Fusion* **59**, 083001 (2019).
 - [11] C. C. Kim, ITPA Meeting (2020).
 - [12] D. Shiraki, N. Commaux, L. R. Baylor, E. N. W., E. M. Hollmann, C. J. Lasnier, and R. A. Moyer, *Phys. Plasmas* **23**, 062516 (2016).
 - [13] L. Chacón, D. Daniel, and W. Taitano, “An asymptotic-preserving 2D-2P relativistic Drift-Kinetic-Equation solver for runaway electron simulations in axisymmetric tokamaks”, *Journal of Computational Physics* , 110772 (2021).
 - [14] C. McDevitt and X. Z. Tang, *European Physics Letters* **217** (2019).
 - [15] M. Yang, G. Zhang, D. del Castillo-Negrete, M. Stoyanov, and M. Beidler, “A sparse-grid probabilistic approximation of the runaway probability of electrons in fusion tokamak simu-

- lations”, <https://arxiv.org/abs/2001.05800> Springer Verlag Lecture Notes (2020).
- [16] M. Yang, G. Zhang, D. del Castillo-Negrete, and M. Stoyanov, “A Feynman-Kac based numerical method for the exit time probability of a class of transport problems”, *Journal of Computational Physics*, 110564 (2021).
- [17] D. del Castillo-Negrete, M. Yang, M. Beidler, and G. Zhang, “Generation and Mitigation of Runaway Electrons: Spatio-Temporal Effects in Dynamic Scenarios”, *Proceedings of the 28th IAEA Fusion Energy Conference* (2021).
- [18] H.-K. Chung, M. Chen, W. Morgan, Y. Ralchenko, and R. Lee, “FLYCHK: Generalized population kinetics and spectral model for rapid spectroscopic analysis for all elements”, *High energy density physics* **1**, 3 (2005).
- [19] O. Sauter, C. Angioni, and Y. R. Lin-Liu, “Neoclassical conductivity and bootstrap current formulas for general axisymmetric equilibria and arbitrary collisionality regime”, *Physics of Plasmas* **6**, 2834 (1999), <https://doi.org/10.1063/1.873240>.
- [20] A. Rechester and M. Rosenbluth, “Electron heat transport in a tokamak with destroyed magnetic surfaces”, *Physical Review Letters* **40**, 38 (1978).
- [21] R. W. Harvey, M. G. McCoy, J. Y. Hsu, and A. A. Mirin, “Electron Dynamics Associated with Stochastic Magnetic and Ambipolar Electric Fields”, *Phys. Rev. Lett.* **47**, 102 (1981).
- [22] M. T. Beidler, D. del Castillo-Negrete, L. R. Baylor, D. Shiraki, and D. A. Spong, *Phys. Plasmas* **27**, 112507 (2020).
- [23] L. Hesslow, O. Embréus, A. Stahl, T. C. DuBois, G. Papp, S. L. Newton, and T. Fülöp, “Effect of Partially Screened Nuclei on Fast-Electron Dynamics”, *Phys. Rev. Lett.* **118**, 255001 (2017).
- [24] E. Hollmann, N. Eidietis, J. Herfindal, P. Parks, A. Pigarov, D. Shiraki, M. Austin, L. Bardoczi, L. Baylor, I. Bykov, T. Carlstrom, D. Kaplan, C. Lasnier, A. Lvovskiy, A. Moser, R. Moyer, C. Paz-Soldan, D. Rudakov, C. Samuell, M. Shafer, M. V. Zeeland, A. Weland, and R. Wilcox, “Study of argon assimilation into the post-disruption runaway electron plateau in DIII-D and comparison with a 1D diffusion model”, *Nucl. Fusion* **59**, 106014 (2019).
- [25] N. Ferraro, Private Communication (2019).
- [26] L. Carbajal, D. del Castillo-Negrete, and J. Martinell, “Runaway electron transport in stochastic toroidal magnetic fields”, *Physics of Plasmas* **27**, 032502 (2020).
- [27] B. Cornille and C. Sovinec, Private Communication (2020).
- [28] S. Munaretto, B. E. Chapman, B. S. Cornille, A. M. DuBois, K. J. McCollam, C. R. Sovinec, A. F. Almagri, and J. A. Goetz, “Generation and suppression of runaway electrons in MST tokamak plasmas”, *Nuclear Fusion* **60**, 046024 (2020).
- [29] B. Cornille, Presented at the DPP meeting of The American Physical Society **Abstract: GO12.00003** (2020).
- [30] B. Lyons and S. Jardin, Private Communication (2020).
- [31] D. Whyte, T. Jernigan, D. Humphreys, A. Hyatt, C. Lasnier, P. Parks, T. Evans, P. Taylor, A. Kellman, D. Gray, and E. Hollmann, “Disruption mitigation with high-pressure noble gas injection”, *Journal of Nuclear Materials* **313-316**, 1239 (2003), *plasma-Surface Interactions in Controlled Fusion Devices* 15.
- [32] L. Carbajal and D. del Castillo-Negrete, “On the synchrotron emission in kinetic simulations

of runaway electrons in magnetic confinement fusion plasmas”, *Plasma Physics and Controlled Fusion* **59**, 124001 (2017).

- [33] Z. Popovic, E. M. Hollmann, D. del Castillo-Negrete, I. Bykov, R. A. Moyer, J. L. Herfindal, D. Shiraki, N. W. Eidietis, C. Paz-Soldan, and A. Lvovskiy, “Polarized imaging of visible synchrotron emission from runaway electron plateaus in DIII-D”, *Physics of Plasmas* **28**, 082510 (2021), <https://doi.org/10.1063/5.0058927>.